Check for updates

JGR Space Physics

RESEARCH ARTICLE
10.1029/2025JA034383

Bridging in Situ Satellite Measurements and Simulations of Magnetic Reconnection Using Recurrent Neural Networks

Cara L. Waters[1], Jonathan P. Eastwood[1], Naïs Fargette[1,2], David L. Newman[3], Martin V. Goldman[3], Martin O. Archer[1], Harry C. Lewis[1], and Harley M. Kelly[1]

[1]Department of Physics, Imperial College London, London, UK, [2]Institut de Recherche en Astrophysique et Planétologie, CNES, Toulouse, France, [3]Center for Integrated Plasma Studies, University of Colorado, Boulder, CO, USA

Key Points:

- We classify spacecraft data into reconnection regions using a neural network trained on particle-in-cell simulation trajectories
- This method reconciles local proxy approaches and full reconstructions by providing structural context without global geometry
- Applied to magnetotail events, the model automatically identifies inflows, outflows, and separatrices, matching prior reconstructions

Correspondence to:
C. L. Waters,
cara.waters18@imperial.ac.uk

Citation:
Waters, C. L., Eastwood, J. P., Fargette, N., Newman, D. L., Goldman, M. V., Archer, M. O., et al. (2025). Bridging in situ satellite measurements and simulations of magnetic reconnection using recurrent neural networks. *Journal of Geophysical Research: Space Physics*, *130*, e2025JA034383. https://doi.org/10.1029/2025JA034383

Received 30 JUN 2025
Accepted 18 SEP 2025

Abstract Magnetic reconnection is inherently structured, with distinct spatial regions such as inflows, outflows, and separatrices playing key roles in energy conversion and particle transport. While in situ spacecraft measurements provide detailed local information, determining where a spacecraft lies within the global reconnection geometry remains a major challenge. Proxy-based methods are often ambiguous, while full reconstructions require strong assumptions and are difficult to apply systematically across events. Here, we present a method that bridges these approaches by using machine learning to infer global structural context from local measurements. We first apply *k*-means clustering to a 2.5-D particle-in-cell simulation to identify six characteristic symmetric reconnection regions. A recurrent neural network (RNN) is then trained on spacecraft-like trajectories through the simulation to classify time series data into these regions. When applied to Magnetospheric Multiscale (MMS) observations of magnetotail reconnection, this method successfully identifies regional transitions, including inflow, outflow, and separatrix crossings, in agreement with previous reconstructions where available. The approach provides a practical, scalable, and automated framework for determining spatial context in reconnection events without requiring full geometric reconstruction, enabling large-scale and efficient statistical studies of reconnection dynamics across multiple events.

Plain Language Summary Magnetic reconnection is a process that rapidly changes the structure of magnetic fields in space and releases large amounts of energy. Spacecraft can measure the detailed properties of the surrounding plasma during reconnection, but it is often difficult to determine where the spacecraft is in relation to the key regions of the reconnection site because the spacecraft can only directly observe the conditions along its trajectory. In this study, we develop a new machine learning-based approach to help solve this problem. First, we use a clustering method to divide a simulation of reconnection into different regions based on the local plasma and field conditions. We then train a type of neural network that can recognize patterns in sequences to learn how simulated spacecraft would pass through these regions. When we apply this trained model to real spacecraft data from Earth's magnetotail, it can automatically identify which region the spacecraft is in at each point in time. This approach provides a new way to understand the structure of reconnection events without needing to reconstruct the full geometry, helping us efficiently study how reconnection behaves across many different cases.

1. Introduction

Magnetic reconnection is a fundamental plasma process that facilitates the rapid reconfiguration of magnetic field lines and the conversion of magnetic energy into kinetic energy, heat, and particle acceleration (Biskamp, 2000, and references therein). The essence of magnetic reconnection is the breaking and rejoining of magnetic field lines, altering the magnetic topology and causing the mixing of previously disconnected plasma regions. Due to this intrinsic dependence on geometry and connectivity, reconnection cannot be fully understood without also understanding the spatial structure in which it occurs. The topology of the magnetic field and its evolution determine not only where reconnection can happen in order to return the field line configuration to a more stable state, but also how energy is redistributed throughout the plasma and the trajectories taken by particles (e.g., Priest & Forbes, 2000; Yamada et al., 2010). Studying this structure is essential for understanding reconnection in astrophysical environments, where it drives phenomena from solar flares to substorms in Earth's magnetosphere (e.g., Birn & Priest, 2007; Zweibel & Yamada, 2009).

In situ spacecraft observations facilitate the direct exploration of local physics within reconnection, especially in near-Earth space (Torbert et al., 2017). The structure of reconnection in these environments is often quasi-two-

© 2025. The Author(s).
This is an open access article under the terms of the Creative Commons Attribution License, which permits use, distribution and reproduction in any medium, provided the original work is properly cited.

21699402, 2025, 10, Downloaded from https://agupubs.onlinelibrary.wiley.com/doi/10.1029/2025JA034383 by Cara Waters - IMPERIAL COLLEGE OF LONDON , Wiley Online Library on [30/09/2025]. See the Terms and Conditions (https://onlinelibrary.wiley.com/terms-and-conditions) on Wiley Online Library for rules of use; OA articles are governed by the applicable Creative Commons License

dimensional, consisting of key regions such as the ion diffusion region (IDR), electron diffusion region (EDR), and the separatrices that demarcate the distinct magnetic domains between the inflows and outflows (Burch et al., 2016; Hesse et al., 1999; Shay et al., 2011). Each region hosts distinct plasma behaviors, and the energetics of the system depend sensitively on location within this structure (Eastwood et al., 2013; Genestreti et al., 2018). Understanding where a spacecraft is located within this framework is therefore critical for interpreting observed physical signatures. This motivates the use of proxies, such as velocity to denote the outflows (e.g., Eastwood et al., 2013), or electron agyrotropy to identify the EDR (Swisdak, 2016), as well as attempts to reconstruct the global structure using multiple spacecraft (probes) or models.

However, proxy-based identification methods, while practical, are often ambiguous due to overlapping signatures (Fargette et al., 2024) and the inherently turbulent and time-dependent nature of reconnection (Genestreti et al., 2023; Stawarz et al., 2024). For example, elevated agyrotropy may indicate proximity to the EDR but can also arise in other kinetic contexts (Aunai et al., 2013), and bulk flow reversals are not unique to outflow regions (Cassak & Shay, 2007; Eastwood et al., 2005). Moreover, in single-spacecraft observations, temporal and spatial variations are entangled, making it difficult to reconstruct the geometry of the reconnection site. Even with multi-spacecraft missions like MMS, reconstruction is limited by the separation scale and trajectory orientation relative to the reconnection structure (Burch et al., 2016; Denton et al., 2018). As a result, the accurate identification of spatial regions within reconnection events remains a major challenge, especially when attempting to generalize across events. This motivates the development of new methodologies that can robustly determine spatial context from observed quantities; either by inferring position within a known structure or reconstructing the structure directly (Hasegawa et al., 2024, and references therein).

To determine the location of a spacecraft relative to a reconnection site, reconstruction methods are often employed to estimate the surrounding field structure. For single-spacecraft observations, two-dimensional and time-independent reconstructions can be applied in regions where the Hall effect is significant, such as the IDR, allowing the spacecraft trajectory to be placed in relation to the X-line (Sonnerup & Teh, 2009). These methods rely on the presence of distinctive field structures along the trajectory, particularly strong electric field gradients, to provide adequate constraints (Sonnerup et al., 2008). The first attempts to recover magnetic field structures from single spacecraft measurements were carried out by integrating a classical Grad-Shafranov equation governing the 2-D magneto-hydrostatic structures in a plasma (Sonnerup & Guo, 1996), and was later applied to the dayside magnetopause (Hau & Sonnerup, 1999). Such methods were subsequently applied successfully to further events at the magnetopause (Hasegawa et al., 2005; Hu & Sonnerup, 2003), the cusp (Hasegawa et al., 2006), in the magnetotail (Hasegawa et al., 2007; Zhang et al., 2007), and in the solar wind (Hu & Sonnerup, 2002).

By finding the motion of a boundary, empirical reconstruction can produce spatial maps showing how quantities vary with position relative to the boundary. For short time intervals where an accurate boundary velocity can be obtained, one-dimensional reconstructions can produce detailed spatial profiles, for example, of the magnetospheric boundary (De Keyser et al., 2005). Two-dimensional reconstruction can provide the geometry of other structures such as flux transfer events, especially with use of multi-spacecraft data (Sibeck et al., 2000).

Three-dimensional reconstructions are also possible using the increased resolution of data from multi-spacecraft missions such as MMS, which is a mission consisting of four identical spacecraft flying in formation (Burch et al., 2016). One common approach involves performing a Taylor expansion of the fields around the barycenter of a tetrahedral spacecraft configuration, such as that provided by MMS (Harvey, 1998). However, this method depends on coordinate systems derived using techniques like the Minimum Directional Derivative (MDD), and may overfit the data, particularly when the X-line lies far from the tetrahedron (Torbert et al., 2020). To mitigate this, reconstructions using only quadratic terms have been proposed, offering improved performance for more distant structures, though at the cost of sensitivity to implementation details and some mismatch with the observed data (Denton et al., 2020). This approach can also be extended by incorporating multiple time steps from the data to reduce overfitting and improve stability (Denton et al., 2022).

Alternative techniques apply additional physical constraints to improve robustness. For example, stochastic optimization methods that incorporate constraints from Maxwell's equations have been used to reconstruct 3-D magnetic fields (Zhu et al., 2022), while electron magnetohydrodynamic (EMHD) reconstructions include terms for dissipation and the divergence of the electron pressure tensor (Hasegawa et al., 2021).

21699402, 2025, 10, Downloaded from https://agupubs.onlinelibrary.wiley.com/doi/10.1029/2025JA034383 by Cara Waters - IMPERIAL COLLEGE OF LONDON , Wiley Online Library on [30/09/2025]. See the Terms and Conditions (https://onlinelibrary.wiley.com/terms-and-conditions) on Wiley Online Library for rules of use; OA articles are governed by the applicable Creative Commons License

In the context of magnetotail reconnection, reconstruction based on kinetic simulation has also proven useful. These approaches compare spacecraft observations with results from particle-in-cell (PIC) simulations to find an optimized trajectory through the simulated domain, minimizing discrepancies in electromagnetic fields, plasma velocities, and pressure tensors (Egedal et al., 2019; Hasegawa et al., 2024). Such methods offer the advantage of providing a reconstruction over a broader region around the X-line.

Nevertheless, reconstruction approaches are event-specific and rely on simplifying assumptions. These may include assumptions of spatial symmetry (e.g., variations in only on direction) (Dunlop & Woodward, 1998), temporal stationarity (Shi et al., 2006), or local dominance of specific plasma regimes such as demagnetized ions and dominant electron dynamics (Sonnerup et al., 2016). Without such assumptions, the methods would not converge to a solution. Coordinate systems must also be calculated for each event, often via methods like Minimum Variance Analysis (MVA), which can introduce their own uncertainties (Sonnerup & Scheible, 1998). Furthermore, reconstruction techniques, particularly those involving optimization, may be computationally demanding.

In this study, we focus on determining the spatial context of MMS observations relative to the structure of magnetic reconnection. Building on previous work using *k*-means clustering to classify regions within a PIC simulation of symmetric reconnection (Waters et al., 2024b), we train a recurrent neural network (RNN) to associate spacecraft-like trajectories with these predefined regions based on time series of plasma and field measurements. This approach allows us to infer which type of region MMS is traversing, such as the inflow, outflow, or separatrix, without requiring the full spatial reconstruction of the reconnection geometry. As such, it serves as a bridge between proxy methods and full reconstruction techniques; it does not provide an exact spatial location within a given region, but it offers a data-driven classification that captures the underlying structure of reconnection. This enables a broader statistical comparison across events, even when reconstruction is not feasible, through an automated and efficient method.

In Section 2, we describe the simulation and spacecraft data used in this study and the data scaling for comparison between the two. Section 3 describes the methods used, including the design of the RNN and optimization of the network parameters. Section 4 then shows application of the trained neural network to four known magnetotail reconnection events of increasing encounter complexity. In each case we evaluate the performance and determine an approximate path of MMS. Section 5 discusses the impacts of these results, and Section 6 provides conclusions, suggesting further applications of this method.

2. Data

This study makes use of both numerical simulation data and in situ spacecraft observations. A two-dimensional particle-in-cell (PIC) simulation of symmetric magnetic reconnection is used to define distinct regions within the reconnection structure based on local plasma and field properties. These regions are then used to train a recurrent neural network (RNN) to classify real spacecraft time series. As always with machine learning applications, it is very important to consider the data preprocessing and the effects of this on the results. Observational data from the Magnetospheric Multiscale (MMS) mission are used to apply and evaluate the method across reconnection events in Earth's magnetotail.

2.1. Particle-in-Cell Simulation

The particle-in-cell simulation of symmetric reconnection with a guide field of $0.1B_0$ uses the iPic3D implicit code (Markidis et al., 2010) starting from a Harris equilibrium, with a mass ratio of $m_i/m_e = 256$, where m_i is the ion mass and m_e the electron mass, at an elapsed time of 24,800 $\omega_{ci}t$ where ω_{ci} is the ion cyclotron frequency. This is the same timestep as described and used in Waters et al. (2024b), with parameters described in Table 1. We crop the simulation to between 130 and 170 d_{i0} in the x_{sim} direction and 20 and 40 d_{i0} in the y_{sim} direction, where d_{i0} is the ion inertial length. This region contains one reconnection site close to the EDR and shows significant extent of the ion outflows.

2.2. Magnetospheric Multiscale (MMS) Data

We use data from the NASA Magnetospheric Multiscale (MMS) mission (Burch et al., 2016) which consists of four identical spacecraft flying in a tetrahedral formation to study magnetic reconnection in Earth's

Table 1
Initial PIC Simulation Parameters

Input parameters	Parameter name	Value
$L_x \times L_y$ (units of d_{i0})	Simulation size	200 × 40
Δ/d_{i0}	Current sheet thickness	0.5
m_i/m_e	Mass ratio	256
v_e/c	Electron velocity ratio	0.045
T_i/T_e	Temperature ratio	5
n_b/n_0	Background to current sheet density	0.1
B_G/B_0	Guide field ratio	0.1

magnetosphere. The four MMS spacecraft and their tetrahedral formation enable multi-spacecraft methods for timing analysis and gradient estimations of the surrounding plasma. Their high-resolution particle moments enable kinetic-scale measurements in magnetic reconnection sites to be sampled. In this study, we focus on events occurring in the magnetotail current sheet, where reconnection commonly occurs. We use plasma moments obtained from the Fast Plasma Investigation (FPI) suite (Pollock et al., 2016), using both ion and electron data products. We use the ion and electron moments in burst mode, the fastest available cadence (150 ms for ions and 30 ms for electrons). Vector magnetic field data are taken from the Fluxgate Magnetometer (FGM) (Russell et al., 2016), using burst mode data at a cadence of 128 vectors per second. Electric field measurements are provided by the Electric Double Probe (EDP) instrument suite (Ergun et al., 2016; Lindqvist et al., 2016; Torbert et al., 2016), and both fast and burst mode data products are used at 32 and 8192 samples per second respectively.

Penetrating radiation (e.g., from solar energetic particle events) can produce an apparent stationary, isotropic population of plasma in the FPI data, affecting both electron and ion measurements. This takes the form of a systematic error and impacts the ion data significantly in the magnetotail as the ambient count rates are low due to the low density. The estimated number density, scalar pressure, and differential energy flux associated with this penetrating radiation are provided as data products. We apply these corrections immediately after loading the data (Gershman et al., 2019).

Photoelectrons may also affect the electron measurements. However, a correction to these is only provided in the form of the velocity distribution function, not to the moments provided, and is automatically applied before the L2 moments are calculated. This model can overestimate the ambient electrons, and cause unphysical moments including zero number density (Liu et al., 2025). An alternative to this is to use partial moment data products. As this work seeks to provide an automated method of processing the data which can be applied quickly, it is therefore impractical to apply such a correction in a suitable manner, as the energy level at which the partial moments should start varies by timestep and is therefore difficult to apply systematically. However, this does result in discrepancies between the ion and electron number densities measured, but, as the normalized electron quantities mostly contribute to the classification of regions only when they are large ($\gg 1$), this has very little effect on the resulting analysis.

For consistency with the simulation-based training data, all vector quantities are converted to the Geocentric Solar Magnetospheric (GSM) coordinate system (as the coordinate system defined by the plane in which magnetotail reconnection occurs is approximately equal to GSM) and normalized using characteristic magnetic field and density values from each event, as described in Section 2.3. Where available, data from all four MMS spacecraft are used to observe differences in the classification results across the formation and infer the difference in trajectories taken. For events after July 2018, MMS4 electron moments are not used due to instrument anomalies affecting two electron spectrometers (Burch et al., 2024).

2.3. Data Normalization

In typical applications of *k*-means clustering, each variable is scaled such that its maximum value is one, ensuring that all variables contribute equally to the clustering process. However, this approach is not feasible when working with spacecraft data. Due to inherently limited sampling along a spacecraft trajectory, we cannot determine the true global maxima of key physical quantities across the entire reconnection region. Instead, we normalize the data using characteristic plasma parameters that are physically meaningful and consistently available. Specifically, we use the reconnecting current sheet ion number density n_0 and the asymptotic reversing magnetic field B_0. From these, we derive the ion and electron Alfvén speeds, V_{Ai0} and V_{Ae0}, respectively,

$$V_{Ai0} = \frac{B_0}{\sqrt{\mu_0 m_i n_0}}, \quad (1)$$

21699402, 2025, 10, Downloaded from https://agupubs.onlinelibrary.wiley.com/doi/10.1029/2025JA034383 by Cara Waters - IMPERIAL COLLEGE OF LONDON , Wiley Online Library on [30/09/2025]. See the Terms and Conditions (https://onlinelibrary.wiley.com/terms-and-conditions) on Wiley Online Library for rules of use; OA articles are governed by the applicable Creative Commons License

$$V_{Ae0} = \frac{B_0}{\sqrt{\mu_0 m_e n_0}}. \quad (2)$$

These provide appropriate scales for normalizing velocities and electric fields.

The electric field is normalized using the ion Alfvén speed (as the bulk plasma motion is predominantly caused by the ions), while the ion and electron velocities are normalized using their respective Alfvén speeds. This ensures that all velocity components across both species are brought to comparable magnitudes, preventing the *k*-means algorithm and the neural network from artificially weighting one species over the other due to differences in scale. For context, the electron Alfvén speed is 16 times larger than that of the ions in the simulation (due to a reduced mass ratio of 256), while for spacecraft data this factor is $\sqrt{1836} \approx 43$.

The resulting normalized quantities are $\mathbf{B}' = \mathbf{B}/B_0$, $n_s' = n_s/n_0$, $\mathbf{E}' = \mathbf{E}/(B_0 V_{Ai0})$, $\mathbf{V}_i' = \mathbf{V}_i/V_{Ai0}$, and $\mathbf{V}_e' = \mathbf{V}_e/V_{Ae0}$, where $\mathbf{B}$ is the magnetic field, n_s is the number density for species s, $\mathbf{E}$ is the electric field, and $\mathbf{V}_i$ and $\mathbf{V}_e$ are the ion and electron bulk velocity vectors. The prime symbol (') denotes that the quantity has been normalized.

3. Methods

To determine where a spacecraft lies within the structure of magnetic reconnection, we develop a machine learning pipeline based on simulation-trained classification. First, we apply *k*-means clustering to a 2.5-D particle-in-cell (PIC) simulation to identify distinct reconnection regions based on local plasma and field parameters. We then generate synthetic trajectories through the simulation domain and use these to train a recurrent neural network (RNN) to recognize sequences of measurements corresponding to different regions. Once trained, the RNN can be applied to time series from MMS to classify each measurement point as belonging to a specific reconnection region. The following subsections describe each component of this approach in detail, including region identification, network design, training, and evaluation.

3.1. Region Identification

Regions are identified using *k*-means clustering in a 14-dimensional parameter space of field and plasma variables in the particle-in-cell (PIC) simulation - $\mathbf{B}$, $\mathbf{E}$, $\mathbf{V}_i$, $\mathbf{V}_e$, n_i and n_e, each scaled as previously described (Waters et al., 2024b). As *k*-means clustering uses the distances between points in the parameter space, the clustering is independent of the coordinate system, provided all variables are in the same orthogonal coordinate system. This means that a specific coordinate system for an event does not need to be found, and any set of data provided in an orthogonal coordinate system can be compared with the clustered simulation. However, later application with the neural network requires simulation and spacecraft data to be in approximately equal coordinate systems. The optimal clustering outcome provides six regions of the simulation—In_N, In_S, Out_E, Out_T, Sep_N, and Sep_S, corresponding to inflows, outflows and separatrices, where the subscripts indicate whether the region is northern, southern, Earthward or tailward compared to a magnetotail reconnection X-line in GSM. These regions are shown in Figure 1a. The EDR is not identified due to the cell size of the simulation being too large in comparison to the electron inertial length, and the IDR is not identified as a separate region due to the majority of the simulation domain used being within the IDR. However, we know that the IDR can be highly structured, and there will be overlap with the separatrices, inflows, and outflows. Further details of this clustering can be found in Waters et al. (2024b).

3.2. Recurrent Neural Networks

To provide the sequential context of a time series and prevent unphysical crossings between regions being identified, a recurrent neural network (RNN) is used. This is a type of artificial neural network that allows information to flow between data steps in the form of internal memory states. A neural network consists of a series of layers of interconnected neurons which each take in values, operate on them using a weight, bias, and activation function, and output the changed value.

Here we use an Elman network, which takes an approach of saving previous computations in a series of context units to then incorporate these in future computations (Elman, 1990). These context units store the parameters of

21699402, 2025, 10, Downloaded from https://agupubs.onlinelibrary.wiley.com/doi/10.1029/2025JA034383 by Cara Waters - IMPERIAL COLLEGE OF LONDON , Wiley Online Library on [30/09/2025]. See the Terms and Conditions (https://onlinelibrary.wiley.com/terms-and-conditions) on Wiley Online Library for rules of use; OA articles are governed by the applicable Creative Commons License

21699402, 2025, 10, Downloaded from https://agupubs.onlinelibrary.wiley.com/doi/10.1029/2025JA034383 by Cara Waters - IMPERIAL COLLEGE OF LONDON , Wiley Online Library on [30/09/2025]. See the Terms and Conditions (https://onlinelibrary.wiley.com/terms-and-conditions) on Wiley Online Library for rules of use; OA articles are governed by the applicable Creative Commons License

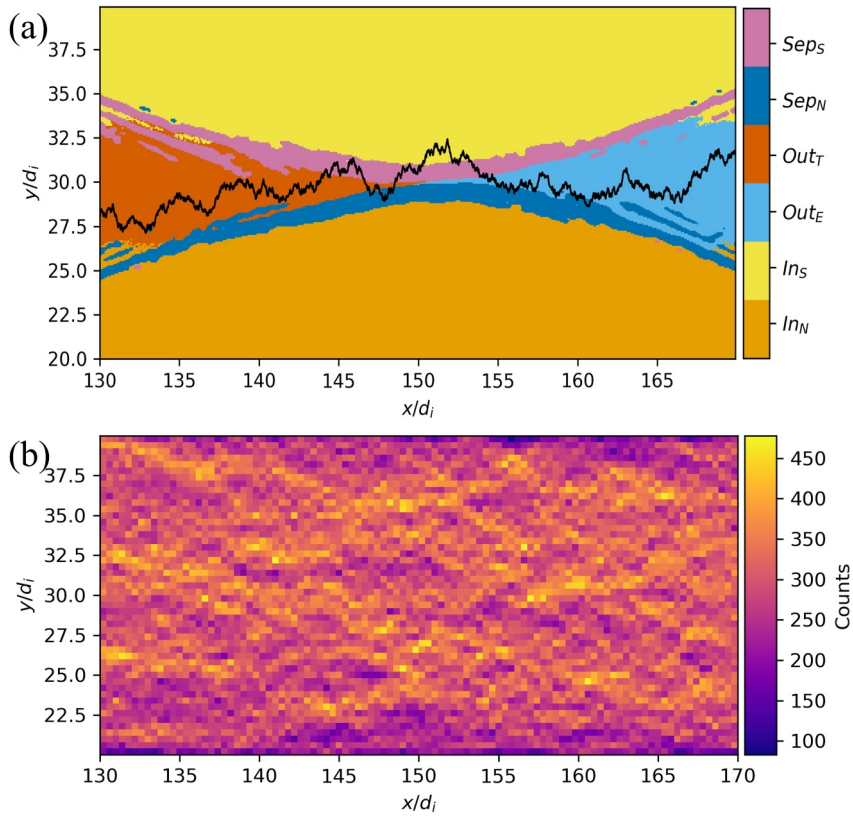

Figure 1. (a) An example of one of the 1,000 emulated spacecraft trajectories generated by a random walk through the simulation space, showing each of the six regions identified by the *k*-means clustering in color and the trajectory as a black line. (b) A 2-D histogram showing the number of points of the generated 1,000 trajectories present in each of the bins.

the hidden neurons from the previous time step, meaning that each timestep is implicitly accounted for in all future computations. These context (memory) units also learn weights for representing the temporal properties of the sequential input. This therefore provides temporal context when applying such a network to spacecraft data. Similar networks have previously been used for other applications within space physics, such as predicting geomagnetic storms (Wu & Lundstedt, 1996) and the AE index (Gleisner & Lundstedt, 2001) successfully.

More recent work has commonly used a long short-term memory (LSTM) network (Hochreiter & Schmidhuber, 1997). However, in this case, we only need a short-term memory about the last handful of points covered by the spacecraft in its trajectory. The simulated trajectories through the spacecraft use a 1-D random walk in the y_{sim} direction. Therefore, to cross more than two grid cells (and change region), only seven random walk steps are required on average (Mosteller et al., 1961). The longer form of short-term memory provided by an LSTM is therefore unnecessary for this application. The simplicity and lower computational cost provided by the Elman network is therefore desirable for the simple temporal dependence of these spacecraft trajectories and the small number of regions being identified. This simplicity also helps to prevent overfitting of the algorithm and to allow fast application of the trained network to new events.

3.3. Training Data

To train our RNN, we require time series-like data as our training set to provide the sequential context required. We assume that reconnection occurring in the simulation and in spacecraft data have reached a steady state and take random walks through the cropped simulation space increasing uniformly by one grid cell in the x_{sim} direction, increasing or decreasing by one grid cell in the y_{sim} direction at each point. This is due to the motion of X-lines primarily retreating in the tail in the $-x_{GSM}$ direction (Oka et al., 2011). A random walk simulates motion that is experienced in the magnetotail, such as flapping of the tail and therefore of the plasma sheet. Each of these random walks is 1,500 steps long. Once the trajectories are generated, Gaussian noise is added to each of them to

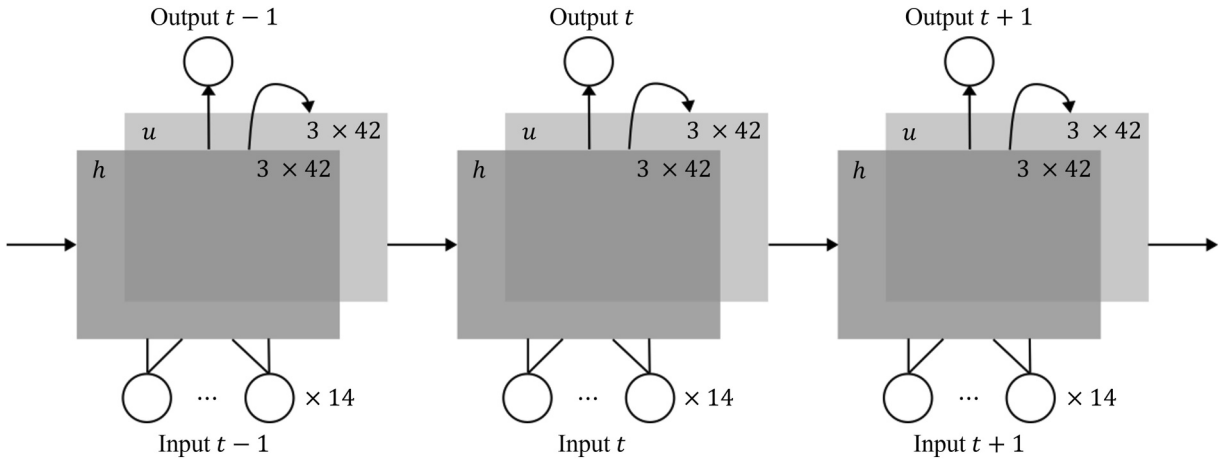

Figure 2. The structure of the recurrent neural network used, with hidden layers h and layers of context neurons u. Each of the 14 input variables at time t are fed in and processed through the three hidden layers before the 42 outputs of the last hidden layer are combined to give one cluster label from a simple linear layer. The context units then feed forward the saved states of the neurons to the next timestep.

simulate noise as a result of for example spacecraft instrument operations. This noise takes random values between 0 and 0.1 for each point in the data set and is added to the existing scaled values assigned from the simulation. We generate 1,000 of these simulated trajectories to form our training set, with an example of one of these shown in Figure 1a.

To confirm whether 1,000 trajectories provide sufficient coverage of the simulation domain, Figure 1b shows the distribution of trajectories. It can be seen that there are at least one hundred trajectories passing through each pixel within the reconnecting regions, giving confidence that the reconnection is well sampled.

To train and optimize, 800 of the generated trajectories were used. 160 of these were set aside for validation, and 640 were used for the initial training. The further 200 trajectories remained for any further required testing of the trained network.

3.4. Network Design

We set up the network as shown in Figure 2, making use of the PyTorch library (Paszke et al., 2019). The input layer takes a 14-dimensional vector for each time step,

$$\mathbf{x}_t = \left[B'_x, B'_y, B'_z, E'_x, E'_y, E'_z, n'_i, n'_e, v'_{ix}, v'_{iy}, v'_{iz}, v'_{ex}, v'_{ey}, v'_{ez}\right] \in \mathbb{R}^{14}. \tag{3}$$

The state of each of the hidden neurons within the layers in the network updates according to the following relation,

$$\mathbf{h}_t = \sigma(\mathbf{W}_h \mathbf{x}_t + \mathbf{U}_h \mathbf{h}_{t-1} + \mathbf{b}_h), \tag{4}$$

where $\mathbf{h}_t$ is the hidden state of size 42 at time t, σ is the activation function, $\mathbf{W}_h$ is a weight matrix of size (42×14) and $\mathbf{U}_h$ is a weight matrix of size (42×42), and $\mathbf{b}_h$ is the bias vector of size 42. The size of these layers is determined by optimization of parameters (see Section 3.5). In this case, the activation function is a tanh function due to it being centered around zero and having a steep gradient between -1 and 1, leading to faster and more efficient training. An Elman network contains three hidden layers by definition.

For the output layer, a fully connected layer maps the hidden state $\mathbf{h}_t$ to the output space,

$$\mathbf{y}_t = \mathbf{W}_o \mathbf{h}_t + \mathbf{b}_o, \tag{5}$$

where $\mathbf{y}_t$ is the output vector of size 6, $\mathbf{W}_o$ is the output weight matrix of size (6×42), and $\mathbf{b}_o$ is the output bias vector of size 6. The outputs are then processed to obtain probabilities of each of the classes from all $\mathbf{y}_t$,

21699402, 2025, 10, Downloaded from https://agupubs.onlinelibrary.wiley.com/doi/10.1029/2025JA034383 by Cara Waters - IMPERIAL COLLEGE OF LONDON , Wiley Online Library on [30/09/2025]. See the Terms and Conditions (https://onlinelibrary.wiley.com/terms-and-conditions) on Wiley Online Library for rules of use; OA articles are governed by the applicable Creative Commons License

$$p_{ij} = \frac{\exp(y_{ij})}{\sum_k \exp(y_{ik})}, \tag{6}$$

where p_{ij} is the probability of class j for sample i. The predicted class is that with the highest probability.

3.5. Network Optimization

The parameters of the network must be optimized. This is carried out until each of the parameters converges. In this case, the parameters optimized are the learning rate (how much the network weights are adjusted for each iteration of training, used by an Adam optimizer (Kingma & Ba, 2014)), the number of hidden units, the dropout rate (the rate at which units are randomly excluded during training to prevent overfitting), and the batch size (the number of samples that are taken to train the network at once). Typically, a larger batch size results in faster training, but poorer generalization of the network.

Optimizing the parameters of the network using the Optuna library (Akiba et al., 2019) resulted in convergence in 144 trials, with the best values for parameters obtained as a learning rate of 1.68×10^{-6}, 42 hidden units per layer, a dropout rate of 3.54×10^{-6}, and a batch size of 32. After assigning these values to the network and training the best model, we find that it reproduces the cluster labels of the remaining 200 test trajectories with 98.0% accuracy.

3.6. Classification Certainty

After obtaining the probability of each of the class assignments from the neural network outputs, we can use the probability associated with the most likely label as a measure of the certainty of the label assignment at that point in time. Overall this probability will be high, as the interfacing of k-means clustering, which applies classifications based on distances from cluster centers, and the RNN, which taken data points and the labels they've been assigned, results in the RNN not knowing the full range of values within the 14-D parameter space. Following visual analysis of the certainties associated with labeling spacecraft data, a certainty of 90% was chosen as a threshold for using a label assignment. If the certainty is below this threshold, no label is assigned for that point in time. For the event of 11 July 2017 (Section 4.1), for each of the four MMS spacecraft, 98.0%, 95.9%, 97.5%, and 96.9% of the points are classified.

3.7. Reliable Time Resolution

We can only consider changes to the region classification which persist for longer than the equivalent time scale of the simulation resolution used to train the neural network. The network cannot reliably inform us of any structure which is occurring at a smaller scale than the PIC simulation cell size. The current sheet density n_0 for each event can be used to calculate the equivalent ion inertial length d_{i0} for each event, which is then used to obtain a time scale using the X-line velocity for the event,

$$t_0 = \frac{c}{12.8 v_{X-line}} \sqrt{\frac{m_i \epsilon_0}{n_0 e^2}}, \tag{7}$$

where v_{X-line} is the overall magnitude of the X-line velocity, and the factor of 12.8 comes from each cell being $(1/12.8)d_{i0}$ in size. This can then be taken as an indication of the minimum timescale for changes in classification that should be considered to be physical. For each event where the X-line velocity has been determined, this is given in Table 2. In most cases, these are not dissimilar to the resolution of measurement provided for ion moments by MMS. However, as data here has been interpolated to the electron cadence, small fluctuations occur faster than these timescales and should be ignored. The classifications are therefore smoothed using a rolling mode with a window size of this reliable timescale for each event.

4. Application to Events

We now turn to the application of the trained recurrent neural network (RNN) to observational data from MMS. Events were selected from the catalogs provided by Rogers et al. (2019, 2023), which identified magnetotail reconnection intervals based on signatures consistent with ongoing reconnection. From this larger catalog, a final

21699402, 2025, 10, Downloaded from https://agupubs.onlinelibrary.wiley.com/doi/10.1029/2025JA034383 by Cara Waters - IMPERIAL COLLEGE OF LONDON , Wiley Online Library on [30/09/2025]. See the Terms and Conditions (https://onlinelibrary.wiley.com/terms-and-conditions) on Wiley Online Library for rules of use; OA articles are governed by the applicable Creative Commons License

21699402, 2025, 10, Downloaded from https://agupubs.onlinelibrary.wiley.com/doi/10.1029/2025JA034383 by Cara Waters - IMPERIAL COLLEGE OF LONDON , Wiley Online Library on [30/09/2025]. See the Terms and Conditions (https://onlinelibrary.wiley.com/terms-and-conditions) on Wiley Online Library for rules of use; OA articles are governed by the applicable Creative Commons License

Table 2
Events Studied Using the Recurrent Neural Network

Start time	End time	B_0 (nT)	n_0 (cm^{-3})	X_{GSM} (R_E)	Y_{GSM} (R_E)	Z_{GSM} (R_E)	$\mathbf{v}_{X-line,GSM}$ (km/s)	t_0 (s)
2017-05-28/03:58:30	2017-05-28/03:59:15	21.3	0.140	−19.3	−11.8	0.79	(71.3, −93.8, 0.5)	0.404
2017-07-06/15:35:10	2017-07-06/15:36:00	16.1	0.439	−24.1	1.41	4.44	(−17.1, 186.8, −42.6)	0.140
2017-07-06/15:46:35	2017-07-06/15:46:52	19.1	0.199	−24.2	1.33	4.48	(−22.3, 66.3, −23.6)	0.541
2017-07-11/22:33:30	2017-07-11/22:34:15	7.81	0.199	−21.5	4.12	3.78	(−122.5, −26.2, 67.4)	0.281
2017-07-17/07:48:45	2017-07-17/07:49:30	16.4	0.173	−18.1	7.30	0.66	(−183.6, 358.9, −35.5)	0.106
2017-07-26/07:00:00[a]	2017-07-26/07:00:45	22.3	0.168	−22.9	8.97	2.28	–	–
2017-07-26/07:28:30[a]	2017-07-26/07:29:15	15.4	0.118	−23.0	8.94	2.20	(80.1, 57.3, 24.9)	0.510
2017-08-23/17:53:30[a]	2017-08-23/17:54:15	17.2	1.32	−18.8	16.1	1.12	–	–
2018-08-27/11:41:00[a]	2018-08-27/11:41:45	15.8	0.211	−21.1	13.3	0.84	(−246.0, 363.2, 160.5)	0.083
2018-08-27/12:15:30	2018-08-27/12:16:00	16.1	0.159	−21.1	13.3	0.97	(−113.7, 209.6, 78.2)	0.178
2018-09-10/17:14:45	2018-09-10/17:15:30	29.1	2.76	−18.2	15.9	1.26	(−410.5, 221.3, −43.9)	0.023
2019-07-25/21:41:10	2019-07-25/21:41:55	10.3	0.204	−24.0	−8.28	4.20	(−209.0, 87.6, 18.6)	0.173
2019-08-31/12:03:00	2019-08-31/12:03:30	32.4	0.710	−13.0	13.3	0.44	(257.7, 13.5, −259.3)	0.058
2019-09-06/04:37:30[a]	2019-09-06/04:41:00	13.3	0.126	−22.0	6.55	−0.93	–	–
2020-08-03/01:05:40	2020-08-03/01:06:20	20.1	0.188	−27.5	−4.90	1.47	(−156.5, 156.5, 57.1)	0.180
2020-08-05/14:18:30[a]	2020-08-05/14:31:00	9.25	0.124	−25.0	2.98	4.59	–	–
2020-08-29/09:55:00[a]	2020-08-29/09:58:00	18.3	0.283	−11.7	11.2	0.92	–	–

[a]Excluded from further analysis due to electron depletion (see Section 4.3).

subset of events was chosen that: (a) exhibits sufficiently complete and high-quality measurements across all required variables; (b) covers a range of spatial trajectories relative to the X-line, including inflow, outflow, and separatrix encounters; and (c) includes both previously studied events and less-analyzed intervals to evaluate the model's performance.

The resulting collection of events is shown in Table 2. Overall, high certainty is achieved for region assignments for all of the events. By running the neural network on this series of events, we are able to qualitatively evaluate the capabilities of the network (which will be discussed further in the context of the case studies). In general, we find that most events cover the reconnection outflows well. The majority of the events also contain encounters with separatrices. However, there are many cases where there may be additional physical phenomena occurring such as turbulence or magnetic islands which cannot be correctly identified due to the simulation used for training providing a very clean case of symmetric and almost anti-parallel reconnection, and this should be taken into account. A small amount of human evaluation is therefore needed to check for such cases.

Case studies of four representative events are shown. These were chosen to illustrate the capabilities and limitations of the method: (a) the 11 July 2017 event has been extensively studied and serves as a benchmark for comparison with reconstruction-based analyses; (b) the 17 July 2017 event is more complex, with strong flapping and multiple current sheet crossings; (c) the 26 July 2017 event demonstrates the impact of data degradation and turbulence; and (d) the 27 August 2018 event, less thoroughly examined in the literature, tests the applicability of the method to less constrained scenarios.

Where prior reconstructions or analyses exist, we summarize the expected region encounters and compare them to the classifications produced by the RNN. This allows the agreement between our method and established interpretations to be evaluated, while also highlighting instances where the model provides additional insight or faces limitations.

4.1. Event of 11 July 2017

The event identified in Torbert et al. (2018) was chosen for initial application of the network due to the number of previous studies and reconstructions. The network produces a cluster label for each time step as in Figure 3.

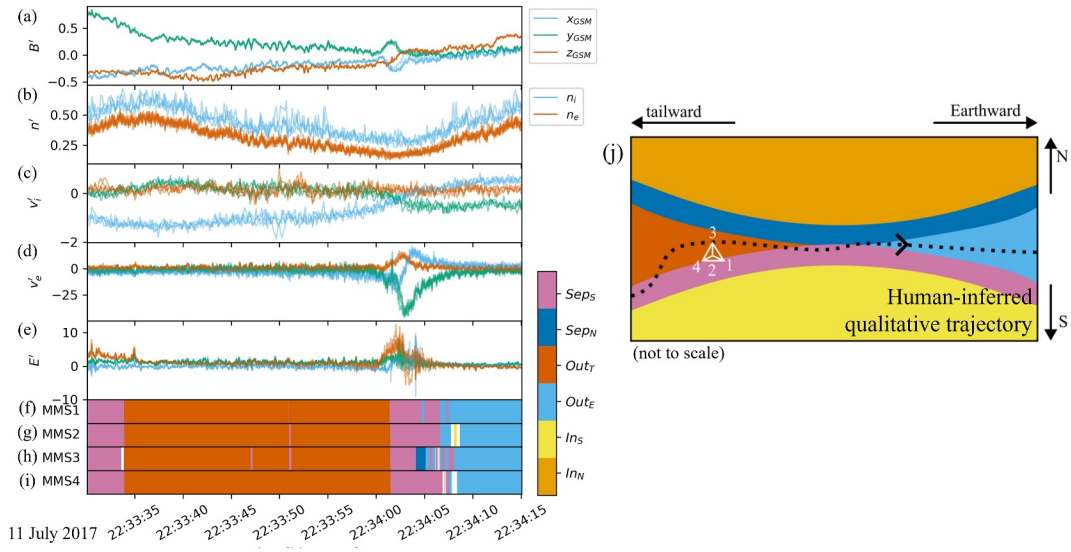

Figure 3. The results of applying the trained recurrent neural network (RNN) to spacecraft data with 14 scaled variables for the magnetotail reconnection event of 11 July 2017. Time series from each of the four MMS spacecraft are plotted together as translucent lines on top of one another, with differences occurring at regions of interest such as surrounding the EDR encounter at 22:34:02. From top to bottom, the panels show (a) scaled magnetic field, (b) number density, (c) ion velocity, (d) electron velocity (here scaled by the ion Alfvén velocity), (e) electric field, (f–i) cluster labels corresponding to each of the spacecraft, and (j) a cartoon of a human-inferred qualitative trajectory through the reconnection site, with the trajectory shown as a black dotted line and the approximate orientation of the MMS tetrahedron in white. This is not to scale, and the trajectory may extend to further away from the X-line than is shown here. Quantities have not had the X-line velocity removed in this plot. Where label certainty is below 90%, no assignment is given and the bar remains white. This indicates that MMS travels through the EDR from the tailward outflow to the earthward outflow, crossing separatrix regions in between.

Here, MMS encountered an EDR where it detected tailward ion and electron bulk velocities followed by earthward flows in both. The observed current sheet features an enhanced current driven by strong out-of-plane electron flows due to the proximity of MMS to the EDR. The guide field ratio B_G/B_0 is estimated to be less than 0.1. Timing differences between the MMS spacecraft in the field and flow reversals shows that the X-line retreated past the spacecraft in the tailward direction. The spacecraft remained close to the neutral sheet except for one brief excursion towards the inflow regions due to flapping of the current sheet around 22:34:00, shown by the small perturbation in the magnetic field components. It is confirmed that MMS encounters both the IDR and EDR through observations of the ion and electron flows. Perpendicular electron flows peaked, returning to be close to the ion velocities around 22:33:50 and 22:34:10 before and after the X-line encounter. A symmetric minimum in the electron number density n_e was observed around the EDR (Torbert et al., 2018).

Many reconstructions of this event have been carried out. Egedal et al. (2019) presented a quantitative comparison between the spacecraft observations and particle-in-cell simulation data. An optimization method was used to find the best set of basis vectors which provided a comparable time series of simulation data to that of the spacecraft data. This provided estimated trajectories showing that MMS3 passed much further into the inner EDR than MMS1, 2, and 4. All four spacecraft approached the X-line from the tailward exhaust, briefly encountering one of the southern separatrices before passing through the EDR and into the Earthward exhaust. An electron MHD reconstruction (Hasegawa et al., 2019) showed that although the X-point was not captured within the tetrahedron of MMS, it did pass as close as one electron inertial length d_e of the X-point. This also shows that MMS3 made the closest approach, passing very close to the X-point, and passing almost directly through the electron stagnation point. This path corresponds closely to that inferred by Nakamura et al. (2019) through multi-spacecraft gradient analysis and the path found as a result of polynomial reconstruction (Denton et al., 2020).

We first study the classification obtained for the data from MMS3, as this is known to make the closest approach to the X-line of this event. MMS3 approached the X-point from the tailward outflow Out_T, close to the southern separatrix Sep_S. As our clustering does not identify the EDR itself (due to the cell size of the simulation used), this region is identified by the crossing between the northern Sep_N and southern Sep_S separatrix regions, before MMS3

21699402, 2025, 10, Downloaded from https://agupubs.onlinelibrary.wiley.com/doi/10.1029/2025JA034383 by Cara Waters - IMPERIAL COLLEGE OF LONDON , Wiley Online Library on [30/09/2025]. See the Terms and Conditions (https://onlinelibrary.wiley.com/terms-and-conditions) on Wiley Online Library for rules of use; OA articles are governed by the applicable Creative Commons License

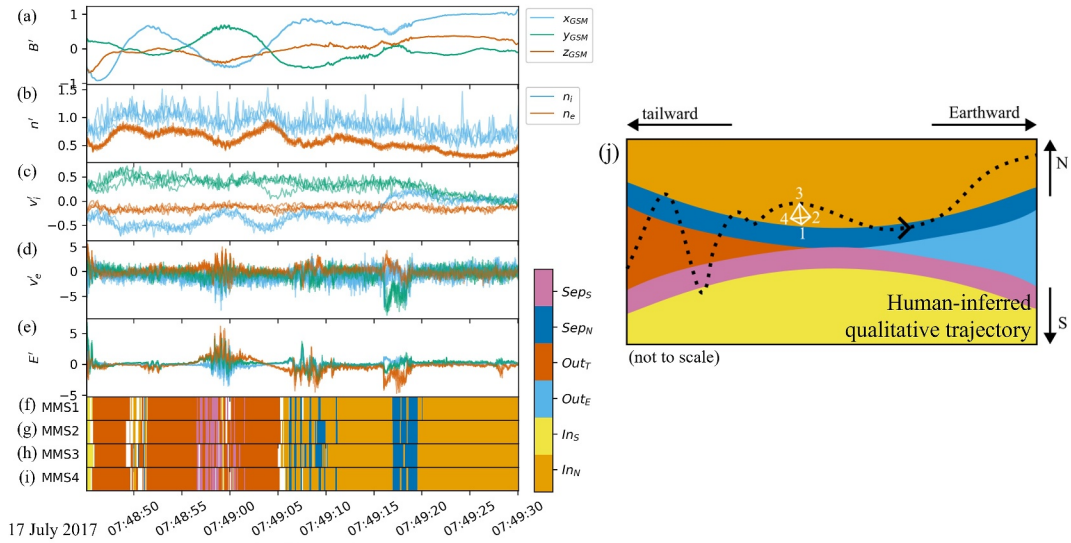

Figure 4. The results of applying the trained recurrent neural network (RNN) to spacecraft data with 14 scaled variables for the magnetotail reconnection event of 17 July 2017. Data is displayed in the same manner as in Figure 3.

was clearly in the Earthward outflow Out_E as the X-line has passed over the spacecraft. This crossing between regions occurs due to the encounter with the electron stagnation point, which in the simulation corresponds closely to the X-point, although this is not the case for this event as found from reconstruction (Hasegawa et al., 2019). MMS1, 2 and 4 did not encounter the northern separatrix region Sep_N, but closely correspond to MMS3 in their other region encounters.

The certainty of assignment drops for the transitions between regions. This is to be expected, as the edges of regions are where different clusters are most similar to each other in parameter space. Overall, the certainties are very close to 100% for the majority of points, indicating a robust method of region assignment. Importantly, the travel between separatrix-associated regions remains after consideration of certainties, confirming with high certainty that MMS3 passed closest to the central X-line. This is further proven by the other three spacecraft not encountering the northern separatrix region Sep_N.

4.2. Event of 17 July 2017

This event (Figure 4) is presented as a case study by Rogers et al. (2019), and occurs on the duskside of the magnetotail. During the overall event encounter, seven current sheet crossings are identified, but in the time period we have chosen to study we observe three. This period was chosen to ensure the ion outflows are still persistent and that the plasma environment being encountered is associated with the reconnection event. Prior to scaling, strong tailward ion flows of approximately 400 km/s are observed throughout the current sheet crossings, reversing to weaker Earthward flows of around 200 km/s following the final current sheet crossing. The ion diffusion region encounter is estimated to occur just after 07:49. Overall, moderate-strength electric fields are observed, including Hall fields in E_z. Three quadrants of the Hall magnetic field are also observed in B_y.

All four of the MMS spacecraft observed very similar features, and therefore we have labels assigned which correspond between all four. Initially, each of the spacecraft traveled from the southern inflow In_S to the tailward outflow Out_T. They then had brief encounters with the southern inflow again, before coming across the southern separatrix region Sep_S. After once again returning to the tailward outflow, the spacecraft crossed over to the northern inflow In_N, and all of them had various encounters with the northern separatrix region Sep_N. As the four spacecraft moved away from the X-line, they remained in the northern inflow. This gives us a clear path through the event, with very few points unable to be classified due to low certainty. However, this is an instance of an event which may be difficult to reconstruct or infer the path of by eye due to the flapping of the current sheet. By using the neural network, we are able to classify the points of the time series despite this complexity.

21699402, 2025, 10, Downloaded from https://agupubs.onlinelibrary.wiley.com/doi/10.1029/2025JA034383 by Cara Waters - IMPERIAL COLLEGE OF LONDON , Wiley Online Library on [30/09/2025]. See the Terms and Conditions (https://onlinelibrary.wiley.com/terms-and-conditions) on Wiley Online Library for rules of use; OA articles are governed by the applicable Creative Commons License

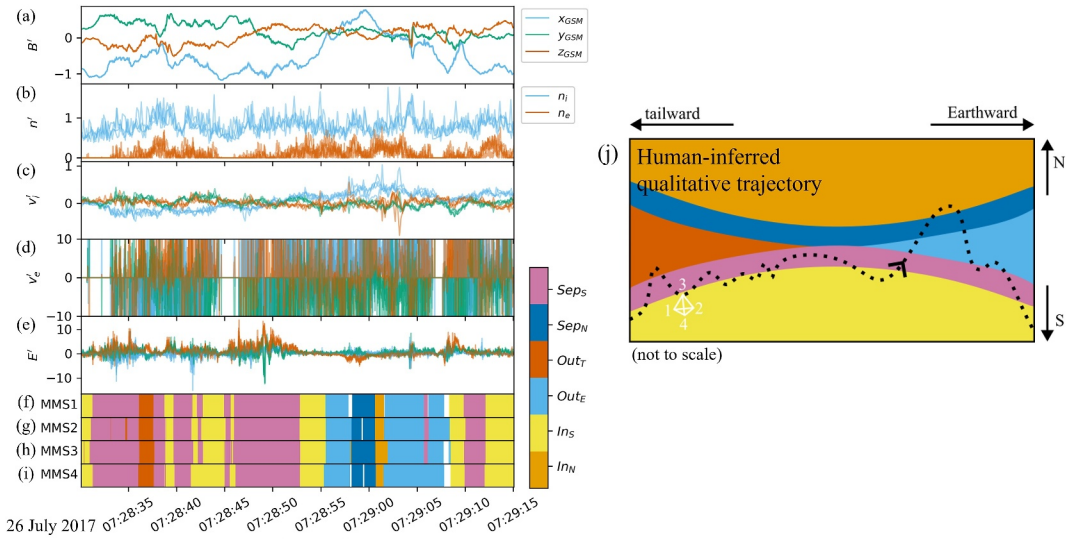

Figure 5. The results of applying the trained recurrent neural network (RNN) to spacecraft data with 14 scaled variables for the magnetotail reconnection event of 26 July 2017. Data is displayed in the same manner as in Figure 3. It is important to note that towards the end of the trajectory, there are crossings between the regions which are either unphysical due to the turbulent nature of the event, or would have to occur much further Earthward of the X-line where the separatrices are no longer significant structures.

4.3. Event of 26 July 2017

This event has been previously studied by Ergun et al. (2018). Here, we see a density-depleted plasma sheet as a result of the ongoing magnetic reconnection. Due to this low density, the ion bulk velocity $\mathbf{v}_i$ may be underestimated, and we see many artifacts in the electron moments n_e and $\mathbf{v}_e$ due to the low counts obtained. In the time period selected, we see strong variations in the magnetic field **B** and the electric field **E**, and taking power spectra of the period indicates that we have strong turbulence. We also see tailward flow followed by earthward flow in the ion velocity, indicating that we are encountering ongoing magnetic reconnection. We can also infer that this is a very active time in the magnetotail, as another reconnection event is encountered approximately half an hour before.

The labels in Figures 5f–5i rapidly fluctuate between regions. This is due to two main problems with the data: the low electron counts making the moments have many artifacts which place the points in significantly different regions in parameter space, and the turbulence which is occurring. As the simulation used is of symmetric reconnection without any additional motion of the X-line occurring or significant turbulence, and the neural network has been trained on simulated trajectories through this, it simply does not have a classification for these turbulent regions. This results in incorrect classification, despite the certainty being high, as the network classifies the points as being in the closest region in parameter space. With the smoothing using the characteristic timescale as detailed in Section 3.7, a trajectory through the event can be inferred. However, we cannot know whether this is accurate or not, especially due to the lack of reliable electron data which is important for accurately determining the separatrix regions. This therefore introduces two limitations to the method—the data must not have significant artifacts due to instrumental effects, and the data must not contain phenomena which differ significantly from those in the simulation used for training. Human input is still currently required to determine whether this is the case. In total, we encounter seven events which present the issue of this electron depletion affecting the moments and these are excluded from further statistical analysis as indicated in Table 2.

4.4. Event of 27 August 2018

We now look at an event which has a much more complex path. This event has been studied in Li et al. (2021), indicating an event with waves driven by meandering electrons, agyrotropic electron velocity distributions, and an electron-scale current sheet. The results of applying the neural network to this event are shown in Figure 6.

21699402, 2025, 10, Downloaded from https://agupubs.onlinelibrary.wiley.com/doi/10.1029/2025JA034383 by Cara Waters - IMPERIAL COLLEGE OF LONDON , Wiley Online Library on [30/09/2025]. See the Terms and Conditions (https://onlinelibrary.wiley.com/terms-and-conditions) on Wiley Online Library for rules of use; OA articles are governed by the applicable Creative Commons License

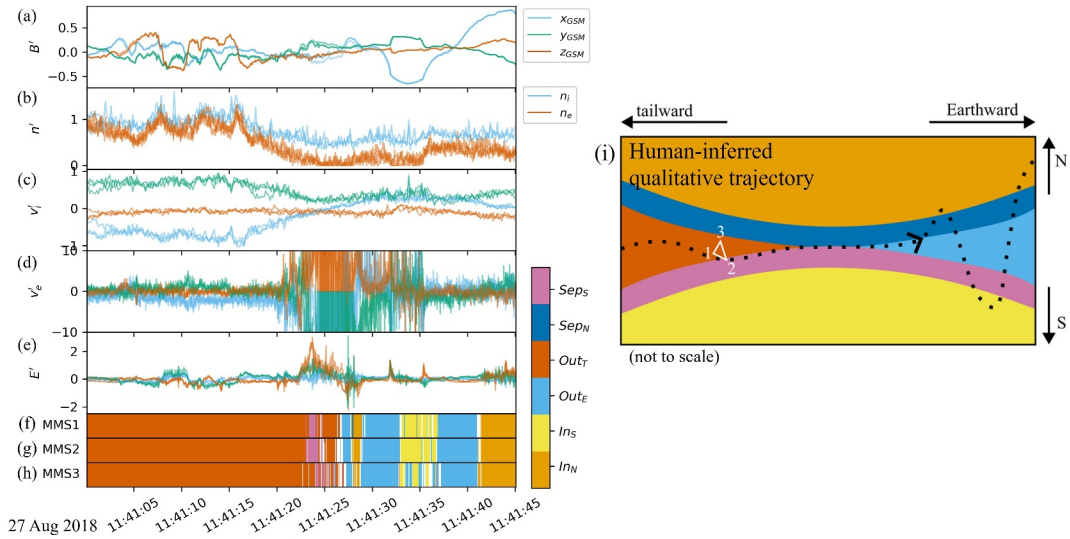

Figure 6. The results of applying the trained recurrent neural network (RNN) to the magnetotail reconnection event of 27 August 2018. Time series from each of the three MMS spacecraft are plotted together. From top to bottom, the panels show (a) scaled magnetic field, (b) number density, (c) ion velocity, (d) electron velocity, (e) electric field, (f–h) cluster labels corresponding to each of the spacecraft, and (i) shows a cartoon of the inferred trajectory, with the trajectory as a black dotted line and part of the MMS tetrahedron in white.

Here, we also encounter issues with the electron data due to the low number density. These issues have been discussed and corrected for thoroughly in Liu et al. (2025), but as discussed in Section 2.2, these corrections will be different for each time step and event and do not lend themselves to being systematically applied with the neural network. However, as we have many periods with sufficient electron data during this event, the electron velocities and the number densities have much lower importance for the cluster assignments than the fields and ion velocities, and we can obtain measures of certainty from the neural network outputs, we can interpret the cluster label assignments after careful consideration of the factors at play. Due to anomalies with the FPI instrument suite on MMS4 following high voltage failures of two electron spectrometer pairs in June and July 2018 and electron moments not being calculated (Burch et al., 2024), we also choose to use data from only three spacecraft.

The path shown by the labels suggests that MMS comes towards the X-line through the tailward outflow Out_T. It then briefly encounters the southern separatrix region Sep_S before crossing over to the earthward outflow Out_E. MMS1 briefly encounters the northern separatrix region Sep_N, before all three spacecraft encounter the northern inflow In_N. We then see a path which could be attributed to flapping of the magnetotail, as all three spacecraft again encounter the earthward outflow Out_E, then the southern inflow In_S, back into the Earthward outflow Out_E, then into the northern inflow In_N. This agrees well with the trajectory through the EDR inferred by Li et al. (2021). However, the interval chosen here extends further away from the X-line, resulting in observations of the current sheet flapping being observed and shown in our trajectory. This explains why the separatrix crossings inferred in Figure 6i due to the classifications crossing directly between inflow and outflow are not seen—these crossings are happening much further down the exhaust, where the separatrices are no longer such significant structures.

From looking at the formation of the constellation at this time, MMS3 was significantly further away from the other two spacecraft, which is consistent with the difference seen in the labels. Only MMS1 sees the northern separatrix region Sep_N for a significant period of time, and MMS2 very briefly encounters it, which is consistent with the slight difference in the observed field components between the spacecraft. This is another example of the strengths of this method, as this is not a clear path which would facilitate reconstruction.

5. Discussion

The method presented here offers a novel approach to determining where a spacecraft lies relative to a reconnection site. By training a recurrent neural network on simulated trajectories through a PIC simulation, we are able

21699402, 2025, 10, Downloaded from https://agupubs.onlinelibrary.wiley.com/doi/10.1029/2025JA034383 by Cara Waters - IMPERIAL COLLEGE OF LONDON , Wiley Online Library on [30/09/2025]. See the Terms and Conditions (https://onlinelibrary.wiley.com/terms-and-conditions) on Wiley Online Library for rules of use; OA articles are governed by the applicable Creative Commons License

21699402, 2025, 10, Downloaded from https://agupubs.onlinelibrary.wiley.com/doi/10.1029/2025JA034383 by Cara Waters - IMPERIAL COLLEGE OF LONDON , Wiley Online Library on [30/09/2025]. See the Terms and Conditions (https://onlinelibrary.wiley.com/terms-and-conditions) on Wiley Online Library for rules of use; OA articles are governed by the applicable Creative Commons License

to classify MMS time series data into regions that represent the underlying structure of magnetic reconnection. This method is particularly useful in cases where conventional reconstruction is challenging, such as when spacecraft trajectories are not well aligned with the expected geometry or when insufficient spatial coverage is available.

Our results show that the region classifications are highly consistent across spacecraft and align well with previous studies that used more intensive reconstruction techniques. For the 11 July 2017 event, in particular, we reproduce the inferred path of MMS3 through the EDR and separatrices with high confidence, consistent with earlier optimization and reconstruction efforts. For more complex or ambiguous events such as 17 July 2017 and 27 August 2018, our method provides a clear regional path even when the field and flow reversals alone would be insufficient to confidently infer the trajectory. This suggests the approach could provide valuable support for interpreting events where traditional analysis by eye or gradient-based methods struggle.

However, this method also has limitations. Because the network is trained on a specific simulation of symmetric reconnection with a modest guide field and relatively steady X-line, it does not generalize well to turbulent conditions or highly asymmetric configurations. This was particularly evident in the 26 July 2017 event, where low electron counts and strong turbulence led to rapid fluctuations in assigned labels that were not physically plausible. This highlights the sensitivity of the method to both data quality (particularly electron moments) and the representativeness of the simulation used in training. Events dominated by dynamics absent in the training set may lead to incorrect classifications with high confidence. Additionally, this method does not aim to determine an exact spatial location within a reconnection structure. It instead provides a categorical classification of region types, such as inflow, outflow, or separatrix, based on statistical similarity in multi-parameter space. In this way, it bridges the gap between proxy-based methods, which rely on individual signatures with known ambiguities, and full reconstruction techniques, which are often difficult to apply systematically. This also makes it suitable for automated large-scale studies, where the goal is to compile statistical trends across many events without needing bespoke reconstruction for each one.

Future extensions of this work could include incorporating a broader variety of training scenarios, such as reconnection with higher guide fields, more turbulence, or asymmetric conditions. Combining this classification method with local proxy indicators could also help refine label certainty or improve performance in data-degraded environments.

6. Conclusions

We present a machine learning method for determining the regional context of spacecraft observations within the structure of magnetic reconnection, using a recurrent neural network trained on particle-in-cell simulation data. This approach enables robust classification of time series data from MMS into regions such as inflows, outflows, and separatrices, without requiring full reconstruction or subjective interpretation.

Applied to several magnetotail reconnection events, the method performs well in identifying expected structures, reproducing paths consistent with prior reconstruction studies, and providing clear classifications even in geometrically complex or ambiguous events. Importantly, it can be applied uniformly across multiple events to build a statistical picture of reconnection dynamics, including how different regions contribute to energy transport.

This technique fills a methodological gap between proxy-based identification and full spatial reconstruction. While it does not resolve precise locations within the reconnection geometry, it offers a reliable and computationally efficient way to determine where in the structure a spacecraft is observing. As such, it opens the door to future large-scale comparative studies of energy partition and dynamics in reconnection events across the magnetosphere through the automation provided. This also facilitates direct comparison between simulation and spacecraft data which has not been previously achieved.

Conflict of Interest

The authors declare no conflicts of interest relevant to this study.

21699402, 2025, 10, Downloaded from https://agupubs.onlinelibrary.wiley.com/doi/10.1029/2025JA034383 by Cara Waters - IMPERIAL COLLEGE OF LONDON , Wiley Online Library on [30/09/2025]. See the Terms and Conditions (https://onlinelibrary.wiley.com/terms-and-conditions) on Wiley Online Library for rules of use; OA articles are governed by the applicable Creative Commons License

Data Availability Statement

The recurrent neural network, along with instructions to utilize it and data generated for the events studied here, can be found at https://github.com/carawaters/mms_rnn_run (Waters, 2025). The recurrent neural network was implemented using the PyTorch library https://pytorch.org (Paszke et al., 2019), version 2.0.1 released 8th May 2023, and optimized using the Optuna library https://github.com/optuna/optuna (Akiba et al., 2019), version 3.3.0 released 7th August 2023. Training and optimization made use of the High Performance Computing (HPC) resources provided by the Research Computing Service at Imperial College London (https://doi.org/10.14469/hpc/2232). Simulation data used to obtain region classifications is available in the *Zenodo* data repository https://doi.org/10.5281/zenodo.12570878 (Waters et al., 2024a). Data from the Magnetospheric Multiscale (MMS) mission (Burch et al., 2016) were used in the creation of this manuscript. MMS data are available at https://lasp.colorado.edu/mms/sdc/public and https://spdf.gsfc.nasa.gov/pub/data/mms/. We use burst mode magnetic field data from FGM on all four spacecraft (Russell et al., 2022a, 2022b, 2022c, 2022d), burst mode electron moments (Gershman et al., 2022a, 2022c, 2022e, 2022g) and ion moments (Gershman et al., 2022b, 2022d, 2022f, 2022h) from FPI on all four spacecraft, and burst and fast mode electric field data from EDP on all four spacecraft (Ergun et al., 2022a, 2022b, 2022c, 2022d, 2022e, 2022f, 2022g, 2022h). The MMS data are archived in the NASA Common Data Format (CDF) and so can be plotted using a number of different data display software packages that parse CDF files. Here, the data analysis was performed using PySPEDAS, an implementation of the Space Physics Environment Data Analysis Software (SPEDAS) framework in Python (Grimes et al., 2022) (https://pyspedas.readthedocs.io/en/latest/), version 1.5.6 released 20th February 2024.

Acknowledgments
CLW was supported by UKRI/STFC studentship ST/X508433/1. Travel benefiting this work was made by CLW with support of a Grant from the Royal Astronomical Society. JPE, NF and HCL were supported by UKRI/STFC Grant ST/W001071/1. MOA was supported by UKRI (STFC/EPSRC) Stephen Hawking Fellowship EP/T01735X/1 and UKRI Future Leaders Fellowship MR/X034704/1. The authors wish to thank the MMS team for their work on the mission. CLW thanks colleagues at Imperial College London for discussions surrounding this work.

References

Akiba, T., Sano, S., Yanase, T., Ohta, T., & Koyama, M. (2019). Optuna: A next-generation hyperparameter optimization framework. In *Proceedings of the 25th ACM SIGKDD international conference on knowledge discovery and data mining* (pp. 2623–2631). Association for Computing Machinery. https://doi.org/10.1145/3292500.3330701

Aunai, N., Hesse, M., Zenitani, S., Kuznetsova, M., Black, C., Evans, R., & Smets, R. (2013). Comparison between hybrid and fully kinetic models of asymmetric magnetic reconnection: Coplanar and guide field configurations. *Physics of Plasmas*, *20*(2), 022902. https://doi.org/10.1063/1.4792250

Birn, J., & Priest, E. R. (2007). *Reconnection of magnetic fields*. Cambridge University Press.

Biskamp, D. (2000). *Magnetic reconnection in plasmas*. Cambridge University Press.

Burch, J. L., Giles, B. L., Ahmadi, N., Argall, M. R., Baker, D. N., Blake, J. B., et al. (2024). Magnetospheric multiscale (MMS)—Calibration and Measurement Algorithms Document (CMAD). *Space Physics Data Facility*. https://doi.org/10.48322/VSHD-SV21

Burch, J. L., Moore, T. E., Torbert, R. B., & Giles, B. L. (2016). Magnetospheric multiscale overview and science objectives. *Space Science Reviews*, *199*(1–4), 5–21. https://doi.org/10.1007/s11214-015-0164-9

Cassak, P. A., & Shay, M. A. (2007). Scaling of asymmetric magnetic reconnection: General theory and collisional simulations. *Physics of Plasmas*, *14*(10), 102114. https://doi.org/10.1063/1.2795630

De Keyser, J., Dunlop, M. W., Owen, C. J., Sonnerup, B. U. O., Haaland, S. E., Vaivads, A., et al. (2005). Magnetopause and boundary layer. *Space Science Reviews*, *118*(1–4), 231–320. https://doi.org/10.1007/s11214-005-3834-1

Denton, R. E., Liu, Y.-H., Hasegawa, H., Torbert, R. B., Li, W., Fuselier, S., & Burch, J. L. (2022). Polynomial reconstruction of the magnetic field observed by multiple spacecraft with integrated velocity determination. *Journal of Geophysical Research: Space Physics*, *127*(10), e2022JA030512. https://doi.org/10.1029/2022JA030512

Denton, R. E., Sonnerup, B. U. O., Russell, C. T., Hasegawa, H., Phan, T. D., Strangeway, R. J., et al. (2018). Determining l-m-n current sheet coordinates at the magnetopause from magnetospheric multiscale data. *Journal of Geophysical Research: Space Physics*, *123*(3), 2274–2295. https://doi.org/10.1002/2017JA024619

Denton, R. E., Torbert, R. B., Hasegawa, H., Dors, I., Genestreti, K. J., Argall, M. R., et al. (2020). Polynomial reconstruction of the reconnection magnetic field observed by multiple spacecraft. *Journal of Geophysical Research: Space Physics*, *125*(2), e2019JA027481. https://doi.org/10.1029/2019JA027481

Dunlop, M. W., & Woodward, T. I. (1998). Multi-spacecraft discontinuity analysis: Orientation and motion. In G. Paschmann & P. W. Daly (Eds.), *Analysis methods for multi-spacecraft data* (pp. 271–305). ESA Publications Division.

Eastwood, J. P., Phan, T. D., Drake, J. F., Shay, M. A., Borg, A. L., Lavraud, B., & Taylor, M. G. G. T. (2013). Energy partition in magnetic reconnection in Earth's magnetotail. *Physical Review Letters*, *110*(22), 225001. https://doi.org/10.1103/PhysRevLett.110.225001

Eastwood, J. P., Sibeck, D. G., Slavin, J. A., Goldstein, M. L., Lavraud, B., Sitnov, M., et al. (2005). Observations of multiple x-line structure in the earth's magnetotail current sheet: A cluster case study. *Geophysical Research Letters*, *32*(11). https://doi.org/10.1029/2005GL022509

Egedal, J., Ng, J., Le, A., Daughton, W., Wetherton, B., Dorelli, J., et al. (2019). Pressure tensor elements breaking the frozen-in law during reconnection in earth's magnetotail. *Physical Review Letters*, *123*(22), 225101. https://doi.org/10.1103/PhysRevLett.123.225101

Elman, J. L. (1990). Finding structure in time. *Cognitive Science*, *14*(2), 179–211. https://doi.org/10.1207/s15516709cog1402_1

Ergun, R. E., Goodrich, K. A., Wilder, F. D., Ahmadi, N., Holmes, J. C., Eriksson, S., et al. (2018). Magnetic reconnection, turbulence, and particle acceleration: Observations in the earth's magnetotail. *Geophysical Research Letters*, *45*(8), 3338–3347. https://doi.org/10.1002/2018GL076993

Ergun, R. E., Lindqvist, P.-A., Torbert, R. B., Ahmadi, N., Graham, D. B., & Burch, J. L. (2022a). Mms 1 Electric Double probe (EDP) three-dimensional electric field, level 2 (L2), burst mode, 0.1220703125 ms data [Dataset]. *NASA Space Physics Data Facility*. https://doi.org/10.48322/rxbn-r719

Ergun, R. E., Lindqvist, P.-A., Torbert, R. B., Ahmadi, N., Graham, D. B., & Burch, J. L. (2022b). Mms 1 Electric Double Probe (EDP) three-dimensional electric field, level 2 (L2), fast mode, 31.25 ms data [Dataset]. *NASA Space Physics Data Facility*. https://doi.org/10.48322/1tgb-hx06

Ergun, R. E., Lindqvist, P.-A., Torbert, R. B., Ahmadi, N., Graham, D. B., & Burch, J. L. (2022c). Mms 2 Electric Double Probe (EDP) three-dimensional electric field, level 2 (L2), burst mode, 0.1220703125 ms data [Dataset]. *NASA Space Physics Data Facility*. https://doi.org/10.48322/pktt-ww31

Ergun, R. E., Lindqvist, P.-A., Torbert, R. B., Ahmadi, N., Graham, D. B., & Burch, J. L. (2022d). Mms 2 Electric Double Probe (EDP) three-dimensional electric field, level 2 (L2), fast mode, 31.25 ms data [Dataset]. *NASA Space Physics Data Facility*. https://doi.org/10.48322/c4r1-p672

Ergun, R. E., Lindqvist, P.-A., Torbert, R. B., Ahmadi, N., Graham, D. B., & Burch, J. L. (2022e). Mms 3 Electric Double Probe (EDP) three-dimensional electric field, level 2 (L2), burst mode, 0.1220703125 ms data [Dataset]. *NASA Space Physics Data Facility*. https://doi.org/10.48322/zn13-qd40

Ergun, R. E., Lindqvist, P.-A., Torbert, R. B., Ahmadi, N., Graham, D. B., & Burch, J. L. (2022f). Mms 3 Electric Double Probe (EDP) three-dimensional electric field, level 2 (L2), fast mode, 31.25 ms data [Dataset]. *NASA Space Physics Data Facility*. https://doi.org/10.48322/tq56-bj65

Ergun, R. E., Lindqvist, P.-A., Torbert, R. B., Ahmadi, N., Graham, D. B., & Burch, J. L. (2022g). Mms 4 Electric Double Probe (EDP) three-dimensional electric field, level 2 (L2), burst mode, 0.1220703125 ms data [Dataset]. *NASA Space Physics Data Facility*. https://doi.org/10.48322/zpw3-4w58

Ergun, R. E., Lindqvist, P.-A., Torbert, R. B., Ahmadi, N., Graham, D. B., & Burch, J. L. (2022h). Mms 4 Electric Double Probe (EDP) three-dimensional electric field, level 2 (L2), fast mode, 31.25 ms data [Dataset]. *NASA Space Physics Data Facility*. https://doi.org/10.48322/dwae-wd67

Ergun, R. E., Tucker, S., Westfall, J., Goodrich, K. A., Malaspina, D. M., Summers, D., et al. (2016). The axial double probe and fields signal processing for the mms mission. *Space Science Reviews*, *199*(1–4), 167–188. https://doi.org/10.1007/s11214-014-0115-x

Fargette, N., Eastwood, J. P., Waters, C. L., Øieroset, M., Phan, T. D., Newman, D. L., et al. (2024). Statistical study of energy transport and conversion in electron diffusion regions at Earth's dayside magnetopause. *Journal of Geophysical Research: Space Physics*, *129*(10), e2024JA032897. https://doi.org/10.1029/2024JA032897

Genestreti, K. J., Farrugia, C. J., Lu, S., Vines, S. K., Reiff, P. H., Phan, T., et al. (2023). Multiscale observation of magnetotail reconnection onset: 1. Macroscopic dynamics. *Journal of Geophysical Research: Space Physics*, *128*(11), e2023JA031758. https://doi.org/10.1029/2023JA031758

Genestreti, K. J., Varsani, A., Burch, J. L., Cassak, P. A., Torbert, R. B., Nakamura, R., et al. (2018). Mms observation of asymmetric reconnection supported by 3-D electron pressure divergence. *Journal of Geophysical Research: Space Physics*, *123*(3), 1806–1821. https://doi.org/10.1002/2017JA025019

Gershman, D. J., Dorelli, J. C., Avanov, L. A., Gliese, U., Barrie, A., Schiff, C., et al. (2019). Systematic uncertainties in plasma parameters reported by the fast plasma investigation on NASA's magnetospheric multiscale mission. *Journal of Geophysical Research: Space Physics*, *124*(12), 10345–10359. https://doi.org/10.1029/2019JA026980

Gershman, D. J., Giles, B. L., Pollock, C. J., Moore, T. E., Kreisler, S., & Burch, J. L. (2022a). Mms 1 fast plasma investigation, dual electron spectrometer (FPI, DES) distribution moments, level 2 (L2), burst mode, 30 ms data [Dataset]. *NASA Space Physics Data Facility*. https://doi.org/10.48322/6172-zw20

Gershman, D. J., Giles, B. L., Pollock, C. J., Moore, T. E., Kreisler, S., & Burch, J. L. (2022b). Mms 1 fast plasma investigation, dual ion spectrometer (FPI, DIS) distribution moments, level 2 (L2), burst mode, 0.15 s data [Dataset]. *NASA Space Physics Data Facility*. https://doi.org/10.48322/qggf-vr83

Gershman, D. J., Giles, B. L., Pollock, C. J., Moore, T. E., Kreisler, S., & Burch, J. L. (2022c). Mms 2 fast plasma investigation, dual electron spectrometer (FPI, DES) distribution moments, level 2 (L2), burst mode, 30 ms data [Dataset]. *NASA Space Physics Data Facility*. https://doi.org/10.48322/tryj-n584

Gershman, D. J., Giles, B. L., Pollock, C. J., Moore, T. E., Kreisler, S., & Burch, J. L. (2022d). Mms 2 fast plasma investigation, dual ion spectrometer (FPI, DIS) distribution moments, level 2 (L2), burst mode, 0.15 s data [Dataset]. *NASA Space Physics Data Facility*. https://doi.org/10.48322/8az2-0h04

Gershman, D. J., Giles, B. L., Pollock, C. J., Moore, T. E., Kreisler, S., & Burch, J. L. (2022e). Mms 3 fast plasma investigation, dual electron spectrometer (FPI, DES) distribution moments, level 2 (L2), burst mode, 30 ms data [Dataset]. *NASA Space Physics Data Facility*. https://doi.org/10.48322/8ypa-ba28

Gershman, D. J., Giles, B. L., Pollock, C. J., Moore, T. E., Kreisler, S., & Burch, J. L. (2022f). Mms 3 fast plasma investigation, dual ion spectrometer (FPI, DIS) distribution moments, level 2 (L2), burst mode, 0.15 s data [Dataset]. *NASA Space Physics Data Facility*. https://doi.org/10.48322/abk8-1g31

Gershman, D. J., Giles, B. L., Pollock, C. J., Moore, T. E., Kreisler, S., & Burch, J. L. (2022g). Mms 4 fast plasma investigation, dual electron spectrometer (FPI, DES) distribution moments, level 2 (L2), burst mode, 30 ms data [Dataset]. *NASA Space Physics Data Facility*. https://doi.org/10.48322/20ws-ge68

Gershman, D. J., Giles, B. L., Pollock, C. J., Moore, T. E., Kreisler, S., & Burch, J. L. (2022h). Mms 4 fast plasma investigation, dual ion spectrometer (FPI, DIS) distribution moments, level 2 (L2), burst mode, 0.15 s data [Dataset]. *NASA Space Physics Data Facility*. https://doi.org/10.48322/vchg-7r51

Gleisner, H., & Lundstedt, H. (2001). Auroral electrojet predictions with dynamic neural networks. *Journal of Geophysical Research*, *106*(A11), 24541–24549. https://doi.org/10.1029/2001JA900046

Grimes, E. W., Harter, B., Hatzigeorgiu, N., Drozdov, A., Lewis, J. W., Angelopoulos, V., et al. (2022). The space physics environment data analysis system in python. *Frontiers in Astronomy and Space Sciences*, *9*, 1020815. https://doi.org/10.3389/fspas.2022.1020815

Harvey, C. C. (1998). Spatial gradients and the volumetric tensor. In G. Paschmann & P. W. Daly (Eds.), *Analysis methods for multi-spacecraft data* (pp. 307–322). ESA Publications Division.

Hasegawa, H., Argall, M. R., Aunai, N., Bandyopadhyay, R., Bessho, N., Cohen, I. J., et al. (2024). Advanced methods for analyzing in-situ observations of magnetic reconnection. *Space Science Reviews*, *220*(6), 68. https://doi.org/10.1007/s11214-024-01095-w

Hasegawa, H., Denton, R. E., Nakamura, R., Genestreti, K. J., Nakamura, T. K. M., Hwang, K., et al. (2019). Reconstruction of the electron diffusion region of magnetotail reconnection seen by the MMS spacecraft on 11 July 2017. *Journal of Geophysical Research: Space Physics*, *124*(1), 122–138. https://doi.org/10.1029/2018JA026051

Hasegawa, H., Nakamura, R., Fujimoto, M., Sergeev, V. A., Lucek, E. A., Rème, H., & Khotyaintsev, Y. (2007). Reconstruction of a bipolar magnetic signature in an earthward jet in the tail: Flux rope or 3D guide-field reconnection? *Journal of Geophysical Research: Space Physics*, *112*(A11). https://doi.org/10.1029/2007JA012492

21699402, 2025, 10, Downloaded from https://agupubs.onlinelibrary.wiley.com/doi/10.1029/2025JA034383 by Cara Waters - IMPERIAL COLLEGE OF LONDON , Wiley Online Library on [30/09/2025]. See the Terms and Conditions (https://onlinelibrary.wiley.com/terms-and-conditions) on Wiley Online Library for rules of use; OA articles are governed by the applicable Creative Commons License

Hasegawa, H., Nakamura, T. K. M., & Denton, R. E. (2021). Reconstruction of the electron diffusion region with inertia and compressibility effects. *Journal of Geophysical Research: Space Physics*, *126*(11), e2021JA029841. https://doi.org/10.1029/2021JA029841

Hasegawa, H., Sonnerup, B. U. O., Klecker, B., Paschmann, G., Dunlop, M. W., & Rème, H. (2005). Optimal reconstruction of magnetopause structures from cluster data. *Annals of Geophysics*, *23*(3), 973–982. https://doi.org/10.5194/angeo-23-973-2005

Hasegawa, H., Sonnerup, B. U. O., Owen, C. J., Klecker, B., Paschmann, G., Balogh, A., & Rème, H. (2006). The structure of flux transfer events recovered from cluster data. *Annals of Geophysics*, *24*(2), 603–618. https://doi.org/10.5194/angeo-24-603-2006

Hau, L.-N., & Sonnerup, B. U. O. (1999). Two-dimensional coherent structures in the magnetopause: Recovery of static equilibria from single-spacecraft data. *Journal of Geophysical Research: Space Physics*, *104*(A4), 6899–6917. https://doi.org/10.1029/1999JA900002

Hesse, M., Schindler, K., Birn, J., & Kuznetsova, M. (1999). The diffusion region in collisionless magnetic reconnection. *Physics of Plasmas*, *6*(5), 1781–1795. https://doi.org/10.1063/1.873436

Hochreiter, S., & Schmidhuber, J. (1997). Long short-term memory. *Neural Computation*, *9*(8), 1735–1780. https://doi.org/10.1162/neco.1997.9.8.1735

Hu, Q., & Sonnerup, B. U. O. (2002). Reconstruction of magnetic clouds in the solar wind: Orientations and configurations. *Journal of Geophysical Research: Space Physics*, *107*(A7). https://doi.org/10.1029/2001JA000293

Hu, Q., & Sonnerup, B. U. O. (2003). Reconstruction of two-dimensional structures in the magnetopause: Method improvements. *Journal of Geophysical Research: Space Physics*, *108*(A1). https://doi.org/10.1029/2002JA009323

Kingma, D. P., & Ba, J. (2014). Adam: A method for stochastic optimization. https://doi.org/10.48550/arXiv.1412.6980

Li, W.-Y., Khotyaintsev, Y. V., Tang, B.-B., Graham, D. B., Norgren, C., Vaivads, A., et al. (2021). Upper-hybrid waves driven by meandering electrons around magnetic reconnection x line. *Geophysical Research Letters*, *48*(16), e2021GL093164. https://doi.org/10.1029/2021GL093164

Lindqvist, P.-A., Olsson, G., Torbert, R. B., King, B., Granoff, M., Rau, D., et al. (2016). The spin-plane double probe electric field instrument for mms. *Space Science Reviews*, *199*(1–4), 137–165. https://doi.org/10.1007/s11214-014-0116-9

Liu, H., Li, W., Tang, B., Norgren, C., Liu, K., Khotyaintsev, Y. V., et al. (2025). High-speed electron flows in the earth magnetotail. *AGU Advances*, *6*(2), e2024AV001549. https://doi.org/10.1029/2024AV001549

Markidis, S., Lapenta, G., & Uddin, R. (2010). Multi-scale simulations of plasma with IPIC3D. *Mathematics and Computers in Simulation*, *80*(7), 1509–1519. https://doi.org/10.1016/j.matcom.2009.08.038

Mosteller, F., Rourke, R. E. K., & Thomas, G. B. (1961). *Probability and statistics*. Addison-Wesley.

Nakamura, R., Genestreti, K. J., Nakamura, T., Baumjohann, W., Varsani, A., Nagai, T., et al. (2019). Structure of the current sheet in the 11 July 2017 electron diffusion region event. *Journal of Geophysical Research: Space Physics*, *124*(2), 1173–1186. https://doi.org/10.1029/2018JA026028

Oka, M., Phan, T. D., Eastwood, J. P., Angelopoulos, V., Murphy, N. A., ieroset, M. O., et al. (2011). Magnetic reconnection x-line retreat associated with dipolarization of the earth's magnetosphere. *Geophysical Research Letters*, *38*(20). https://doi.org/10.1029/2011GL049350

Paszke, A., Gross, S., Massa, F., Lerer, A., Bradbury, J., Chanan, G., et al. (2019). Pytorch: An imperative style, high-performance deep learning library. In H. Wallach, H. Larochelle, A. Beygelzimer, F. d'Alché-Buc, E. Fox, & R. Garnett (Eds.), *Advances in neural information processing systems* (Vol. 32). Curran Associates, Inc. Retrieved from https://proceedings.neurips.cc/paper_files/paper/2019/file/bdbca288fee7f92f2bfa9f7012727740-Paper.pdf

Pollock, C., Moore, T., Jacques, A., Burch, J., Gliese, U., Saito, Y., et al. (2016). Fast plasma investigation for magnetospheric multiscale. *Space Science Reviews*, *199*(1–4), 331–406. https://doi.org/10.1007/s11214-016-0245-4

Priest, E. R., & Forbes, T. G. (2000). *Magnetic reconnection: MHD theory and applications*. Cambridge University Press.

Rogers, A. J., Farrugia, C. J., & Torbert, R. B. (2019). Numerical algorithm for detecting ion diffusion regions in the geomagnetic tail with applications to mms tail season 1 May to 30 September 2017. *Journal of Geophysical Research: Space Physics*, *124*(8), 6487–6503. https://doi.org/10.1029/2018JA026429

Rogers, A. J., Farrugia, C. J., Torbert, R. B., & Rogers, T. J. (2023). Applying magnetic curvature to mms data to identify thin current sheets relative to tail reconnection. *Journal of Geophysical Research: Space Physics*, *128*(1), e2022JA030577. https://doi.org/10.1029/2022JA030577

Russell, C. T., Anderson, B. J., Baumjohann, W., Bromund, K. R., Dearborn, D., Fischer, D., et al. (2016). The magnetospheric multiscale magnetometers. *Space Science Reviews*, *199*(1–4), 189–256. https://doi.org/10.1007/s11214-014-0057-3

Russell, C. T., Magnes, W., Wei, H., Bromund, K. R., Plaschke, F., Fischer, D., et al. (2022a). Mms 1 flux gate magnetometer (FGM) dc magnetic field, level 2 (L2), burst mode, 128 sample/s, v4/5 data [Dataset]. *NASA Space Physics Data Facility*. https://doi.org/10.48322/pj0n-m695

Russell, C. T., Magnes, W., Wei, H., Bromund, K. R., Plaschke, F., Fischer, D., et al. (2022b). Mms 2 flux gate magnetometer (FGM) dc magnetic field, level 2 (L2), burst mode, 128 sample/s, v4/5 data [Dataset]. *NASA Space Physics Data Facility*. https://doi.org/10.48322/ggx2-zg64

Russell, C. T., Magnes, W., Wei, H., Bromund, K. R., Plaschke, F., Fischer, D., et al. (2022c). Mms 3 flux gate magnetometer (FGM) dc magnetic field, level 2 (L2), burst mode, 128 sample/s, v4/5 data [Dataset]. *NASA Space Physics Data Facility*. https://doi.org/10.48322/y55w-eb74

Russell, C. T., Magnes, W., Wei, H., Bromund, K. R., Plaschke, F., Fischer, D., et al. (2022d). Mms 4 flux gate magnetometer (FGM) dc magnetic field, level 2 (L2), burst mode, 128 sample/s, v4/5 data [Dataset]. *NASA Space Physics Data Facility*. https://doi.org/10.48322/257w-3j79

Shay, M. A., Drake, J. F., Eastwood, J. P., & Phan, T. D. (2011). Super-Alfvénic propagation of substorm reconnection signatures and poynting flux. *Physical Review Letters*, *107*(6), 065001. https://doi.org/10.1103/PhysRevLett.107.065001

Shi, Q. Q., Shen, C., Dunlop, M. W., Pu, Z. Y., Zong, Q.-G., Liu, Z. X., et al. (2006). Motion of observed structures calculated from multi-point magnetic field measurements: Application to cluster. *Geophysical Research Letters*, *33*(8). https://doi.org/10.1029/2005GL025073

Sibeck, D. G., Prech, L., Safrankova, J., & Nemecek, Z. (2000). Two-point measurements of the magnetopause: Interball observations. *Journal of Geophysical Research: Space Physics*, *105*(A1), 237–244. https://doi.org/10.1029/1999JA900390

Sonnerup, B. U. O., & Guo, M. (1996). Magnetopause transects. *Geophysical Research Letters*, *23*(25), 2679–3682. https://doi.org/10.1029/96GL03573

Sonnerup, B. U. O., Hasegawa, H., Denton, R. E., & Nakamura, T. K. M. (2016). Reconstruction of the electron diffusion region. *Journal of Geophysical Research: Space Physics*, *121*(5), 4279–4290. https://doi.org/10.1002/2016JA022430

Sonnerup, B. U. O., & Scheible, M. (1998). Minimum and maximum variance analysis. In G. Paschmann & P. W. Daly (Eds.), *Analysis methods for multi-spacecraft data* (pp. 185–220). ESA Publications Division.

Sonnerup, B. U. O., & Teh, W.-L. (2009). Reconstruction of two-dimensional coherent structures in ideal and resistive hall MHD: The theory. *Journal of Geophysical Research: Space Physics*, *114*(A4). https://doi.org/10.1029/2008JA013897

Sonnerup, B. U. O., Teh, W.-L., & Hasegawa, H. (2008). Grad-Shafranov and MHD reconstructions. In G. Paschmann & P. W. Daly (Eds.), *Multi-spacecraft analysis methods revisited* (pp. 81–90). ESA Communications.

Stawarz, J. E., Muñoz, P. A., Bessho, N., Bandyopadhyay, R., Nakamura, T. K. M., Eriksson, S., et al. (2024). The interplay between collisionless magnetic reconnection and turbulence. *Space Science Reviews*, *220*(90), 90. https://doi.org/10.1007/s11214-024-01124-8

21699402, 2025, 10, Downloaded from https://agupubs.onlinelibrary.wiley.com/doi/10.1029/2025JA034383 by Cara Waters - IMPERIAL COLLEGE OF LONDON , Wiley Online Library on [30/09/2025]. See the Terms and Conditions (https://onlinelibrary.wiley.com/terms-and-conditions) on Wiley Online Library for rules of use; OA articles are governed by the applicable Creative Commons License

Swisdak, M. (2016). Quantifying gyrotropy in magnetic reconnection. *Geophysical Research Letters*, *43*(1), 43–49. https://doi.org/10.1002/2015GL066980

Torbert, R. B., Burch, J. L., Argall, M. R., Alm, L., Farrugia, C. J., Forbes, T. G., et al. (2017). Structure and dissipation characteristics of an electron diffusion region observed by mms during a rapid, normal-incidence magnetopause crossing. *Journal of Geophysical Research: Space Physics*, *122*(12), 11901–11916. https://doi.org/10.1002/2017JA024579

Torbert, R. B., Burch, J. L., Phan, T. D., Hesse, M., Argall, M. R., Shuster, J., et al. (2018). Electron-scale dynamics of the diffusion region during symmetric magnetic reconnection in space. *Science*, *362*(6421), 1391–1395. https://doi.org/10.1126/science.aat2998

Torbert, R. B., Dors, I., Argall, M. R., Genestreti, K. J., Burch, J. L., Farrugia, C. J., et al. (2020). A new method of 3-d magnetic field reconstruction. *Geophysical Research Letters*, *47*(3), e2019GL085542. https://doi.org/10.1029/2019GL085542

Torbert, R. B., Russell, C. T., Magnes, W., Ergun, R. E., Lindqvist, P.-A., Le Contel, O., et al. (2016). The fields instrument suite on mms: Scientific objectives, measurements, and data products. *Space Science Reviews*, *199*(1–4), 105–135. https://doi.org/10.1007/s11214-014-0109-8

Waters, C. L. (2025). mms_rnn_run. https://doi.org/10.5281/zenodo.15723061

Waters, C. L., Eastwood, J. P., Fargette, N., Newman, D. L., & Goldman, M. V. (2024a). 2.5-d pic simulation of symmetric magnetic reconnection with varying guide field [Dataset]. *Zenodo*. https://doi.org/10.5281/zenodo.12570878

Waters, C. L., Eastwood, J. P., Fargette, N., Newman, D. L., & Goldman, M. V. (2024b). Classifying magnetic reconnection regions using *k*-means clustering: Applications to energy partition. *Journal of Geophysical Research: Space Physics*, *129*(10), e2024JA033010. https://doi.org/10.1029/2024JA033010

Wu, J.-G., & Lundstedt, H. (1996). Prediction of geomagnetic storms from solar wind data using Elman recurrent neural networks. *Geophysical Research Letters*, *23*(4), 319–322. https://doi.org/10.1029/96GL00259

Yamada, M., Kulsrud, R., & Ji, H. (2010). Magnetic reconnection. *Reviews of Modern Physics*, *82*(1), 603–664. https://doi.org/10.1103/RevModPhys.82.603

Zhang, Y. C., Liu, Z. X., Shen, C., Fazakerley, A., Dunlop, M., me, H. R., et al. (2007). The magnetic structure of an earthward-moving flux rope observed by cluster in the near-tail. *Annals of Geophysics*, *25*(7), 1471–1476. https://doi.org/10.5194/angeo-25-1471-2007

Zhu, X., Cohen, I. J., Mauk, B. H., Nikoukar, R., Turner, D. L., & Torbert, R. B. (2022). A new three-dimensional empirical reconstruction model using a stochastic optimization method. *Frontiers in Astronomy and Space Sciences*, *9*, 878403. https://doi.org/10.3389/fspas.2022.878403

Zweibel, E. G., & Yamada, M. (2009). Magnetic reconnection in astrophysical and laboratory plasmas. *Annual Review of Astronomy and Astrophysics*, *47*(1), 291–332. https://doi.org/10.1146/annurev-astro-082708-101726

21699402, 2025, 10, Downloaded from https://agupubs.onlinelibrary.wiley.com/doi/10.1029/2025JA034383 by Cara Waters - IMPERIAL COLLEGE OF LONDON , Wiley Online Library on [30/09/2025]. See the Terms and Conditions (https://onlinelibrary.wiley.com/terms-and-conditions) on Wiley Online Library for rules of use; OA articles are governed by the applicable Creative Commons License